Continental Shelf Research 225 (2021) 104474

Contents lists available at ScienceDirect

Continental Shelf Research

journal homepage: www.elsevier.com/locate/csr

Propagation and amplification of meteotsunamis in multiple harbors along the eastern Yellow Sea coast

Myung-Seok Kim, Seung-Buhm Woo *

Department of Ocean Sciences, Inha University, Incheon, 22212, Republic of Korea

ARTICLE INFO

Keywords:
Meteotsunamis
Air pressure disturbances
Wave propagation
Amplification
Proudman resonance
Harbor resonance

ABSTRACT

This study investigates the propagation and principal resonance characteristics of meteorological tsunamis (i.e., meteotsunamis) along the eastern Yellow Sea coast, which were anomalously strong in multiple harbors on April 25–26, 2008. Meteorological and sea level data were used to examine the link between atmospheric disturbances and meteotsunamis, and meteorological images were collected to estimate the propagation of atmospheric disturbances. Significant tsunami-like sea level oscillations were sequentially detected at the harbor tide gauges with increased spectral energy within broad period bands of less than 30 min, containing the fundamental period of each harbor. Meteorological parameters indicating the passage of a squall line, such as air pressure disturbances, wind disturbances, high rain rates, and lightning strikes, were also observed. The long ocean waves forced by the propagating squall line generated internal resonances, causing local amplification in multiple harbors. It appears that meteotsunami-induced harbor seiches were generated. Our results demonstrated that the pressure-forced meteotsunamis propagated toward the entrance of the harbors located on the propagation path, resulting in additional amplification by harbor resonance after the Proudman resonance amplifying the long waves in the open sea. The resonance characteristics favorable to additional amplification are the propagation of intense air pressure disturbances, harbors with large quality factors, and dominant period bands of the incoming long waves. The proposed resonance characteristics of specific sites can help in improving the accuracy of the current meteotsunami monitoring system in the Yellow Sea.

1. Introduction

Seiches and harbor oscillations induced by direct external forcings (e.g., air pressure disturbances, wind gusts, and seismic activity) in enclosed basins and atmospherically generated long ocean waves entering the corresponding harbors are free and forced oscillations (Rabinovich, 2009). Normal free oscillations without external forcing redistribute the energy due to wave interference or local topographical effects. Contrastingly, the extreme pressure-forced seiches, which are also called meteotsunamis, are forced oscillations that can obtain additional energy from the coupled-mode propagation with air pressure disturbances (Monserrat et al., 2006). Air pressure disturbances are associated with various atmospheric disturbances, such as dynamic instability, orographic influence, frontal passages, gales, squalls, storms, tornadoes, convection cells, and atmospheric gravity waves (Gossard and Hooke, 1975). Meteotsunamis have been reported worldwide, particularly in England, Spain, Croatia, Australia, Japan, and USA (Rabinovich, 2020; Vilibić et al., 2014). Large meteotsunami-induced harbor seiches are characterized as sequential amplification by harbor resonances of the Balearic Islands following the traveling air pressure disturbances in the open sea (Garcies et al., 1996; Gomis et al., 1993). Multi-resonance phenomenon (Pattiaratchi and Wijeratne, 2015) have occurred across several southern European countries over a distance of thousands of kilometers in the form of widespread tsunami-like waves of atmospheric origin (Šepić et al., 2015b). The traveling air pressure disturbances of approximately 3 hPa propagated by resonance coupling can lead to destructive meteotsunamis in bays and harbors amplified up to several meters (Hibiya and Kajiura, 1982). Therefore, understanding the resonance characteristics of meteotsunamis is important for monitoring hazardous oscillations in semi-closed basins.

Strong amplification of the meteotsunami is the result of a resonance mechanism (Rabinovich, 2009). It is also called a double resonance effect, which indicates external resonance between the propagating air pressure disturbances and resultant sea level oscillations in the open sea followed by internal resonance between the incoming long waves toward the harbor entrance and fundamental mode of the harbor

* Corresponding author.
E-mail address: sbwoo@inha.ac.kr (S.-B. Woo).

https://doi.org/10.1016/j.csr.2021.104474
Received 29 November 2020; Received in revised form 24 May 2021; Accepted 26 May 2021
Available online 1 June 2021
0278-4343/© 2021 Published by Elsevier Ltd.

(Monserrat et al., 2006). To date, previous studies based on observations and numerical simulations have primarily focused on the first step of the resonance mechanism due to the coupled mode between the atmospheric disturbance and forced progressive wave, which is called the Proudman resonance (Belušić et al., 2007; Chen and Niu, 2018; Proudman, 1929; Vilibić, 2008; Vilibić et al., 2004). This is because favorable conditions for the generation of the first resonance mechanism (e.g., intensity, speed, and direction of the atmospheric disturbance) are the key factors in determining the disturbance pathway and potential amplitude of the meteotsunamis on the continental shelf (Pattiaratchi and Wijeratne, 2015; Šepić et al., 2015a). Unlike pre-amplified long waves that are normally several centimeters high and thus unnoticeable in the open sea, additionally amplified waves in bays, inlets, and harbors with narrow entrances can become several meters high, thereby destroying boats and seriously injuring or killing people (Monserrat et al., 2006; Rabinovich, 2009). The second step of the resonance mechanism is also crucial for the prediction and monitoring of the maximum wave heights in semi-closed basins, as it determines whether the forced progressive waves were amplified up to the warning level for destructive meteotsunamis. Nevertheless, the generation of additional resonance and its favorable conditions in semi-closed basins after the Proudman resonance have yet to be quantitatively examined in previous studies.

Monitoring possibility of double resonance effect has been suggested to detect the meteotsunamis (i.e., forced waves) before the intense amplification that can cause destructive harbor seiches (Ozsoy et al., 2016; Šepić and Vilibić, 2011; Šepić et al., 2009b, 2016; Vilibić et al., 2018). Because of pressure-forced meteotsunamis in bays and harbors located along the eastern Yellow Sea coast, severe human casualties and property damage (e.g., ship loss, fish farm loss, and flooding) were reported on March 31, 2007, May 4, 2008, and April 26, 2011 (Kim et al., 2019). Accordingly, a real-time air pressure disturbance monitoring system was developed to detect the potential meteotsunamis in the Yellow Sea (Kim et al., 2021). However, the monitoring system was operated primarily based on the characteristics of the air pressure disturbance related to external resonance. Additionally, the parameters related to internal resonance were not considered, and this can partly contribute to false-positive problems (air pressure disturbances were detected but meteotsunamis did not occur). Although the origin of atmospheric disturbances and the first step of the resonance mechanism of the reported meteotsunami events in the Yellow Sea have been assessed (Choi and Lee, 2009; Choi et al., 2008; Eom et al., 2012; Kim et al., 2014), additional amplification in the basin has not been considered. It is expected that the hurdle in the monitoring system can be solved by additionally considering the specific resonance characteristics of the basin favorable to the generation of internal resonance.

The focus of this study is to investigate the propagation and amplification of tsunami-like sea level oscillations along the eastern Yellow Sea coast on April 25, 2008. In particular, we aim to quantify the resonance characteristics of multiple harbors where significant amplification occurred for supplementing the monitoring system in operation. First, the characteristics of the sea level oscillations and origin of atmospheric disturbances were examined using air pressure, wind, sea level, and meteorological image data covering a large area along the eastern Yellow Sea coast. Second, correlation in the time-frequency domain and the propagation patterns were analyzed to identify the coupled mode between atmospheric disturbances and meteotsunamis. Finally, the characteristics of the local amplification in each basin were assessed after the external resonance due to coupled-mode propagation.

2. Data and methods

2.1. Data

Meteorological data were collected through land-based automatic weather stations (AWSs) operated by the Korea Meteorological Administration (KMA). Mean sea level pressure and wind, which are available at 1 min intervals, were examined from 09:00 to 09:00 KST (Korean Standard Time, UTC+9) on April 25–26, 2008. Atmospheric disturbances were analyzed using 126 AWSs, including 23 coastal AWSs, which exceeded the air pressure disturbance limit (2 hPa/10 min) indicating the rate of pressure change (Šepić and Vilibić, 2011; Šepić et al., 2009b). The remaining 103 AWSs were located inland areas (Fig. 1). The surface pressure chart at 3 h intervals, rain rate at 10 min intervals, and lightning strike at 10 min intervals provided by the KMA were utilized to cross-check the spatial and temporal propagation of the air pressure disturbances, which were derived from the 23 AWSs. In addition, we used tide gauge records, which are operated by the Korea Hydrographic and Oceanographic Agency (KHOA), on April 23–27, 2008, to assess the high-frequency sea level oscillations along the eastern Yellow Sea coast (Fig. 1). The sea levels at 1 min intervals were obtained from 10 tide gauges. Excluding the Wido (WD) tide gauge that measures the sea levels with microwave radars, the remaining nine tide gauges were observed with the floating buoys in the tide wells. Each buoy was connected to a well pipe with a specific diameter to filter out the energetic oscillations caused by wind waves. Therefore, swell-induced oscillations were considered to have already been removed during the sampling process. The abbreviations for each station are listed in Table 1.

2.2. Wavelet analysis

Wavelet analysis was used for the study of meteorological and sea level data showing non-stationarity. The wavelet transform $WT(n,s)$ of a certain variable can be expressed by converting the raw time series $x(t)$ into the time-frequency domain, as shown in Eq. (1):

$$WT(n,s)=\frac{1}{\sqrt{s}}\int \psi^{*}\left(\frac{t-n}{s}\right)x(t)dt \tag{1}$$

where n is the time index, s is the scale, and ψ^{*} is the complex conjugate of the basis function. The wavelet transform was performed using a Morlet wavelet basis function, which is useful for detecting dynamic variability of disturbances for various research areas such as climate index, earthquake, image, and turbulence analysis (Thomson and Emery, 2014). Finally, the variability of atmospheric disturbances and sea level oscillations over time and period was examined by calculating the wavelet power spectrum (WPS) $|WT(n,s)|^2$ with the wavelet transform $WT(n, s)$. After the wavelet transform, a wavelet filter and scale-averaged wavelet power (SAWP) were used to extract the time series of interest and examine the time series of the average variance, respectively (Torrence and Compo, 1998). In addition, the correlation between atmospheric disturbance and sea level oscillation was examined by the cross-wavelet power spectrum (XWPS) with the cross-wavelet transform (Grinsted et al., 2004), as expressed in Eq. (2):

$$XWPS(n,s)=\frac{\left|WT_X(n,s)WT_Y^{*}(n,s)\right|}{\sigma_X\sigma_Y} \tag{2}$$

where σ_X and σ_Y are the standard deviations for each variable. Based on

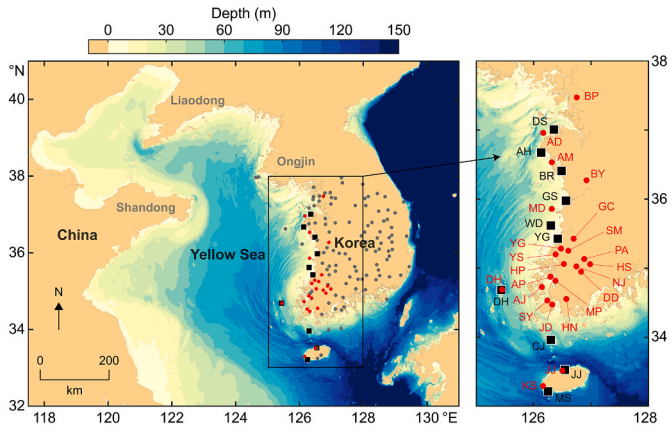


Fig. 1. Map showing observation locations and bathymetry of the Yellow Sea. The square and circle symbols show 10 tide gauges and 126 automatic weather stations (AWSs), respectively. The red circles indicate the 23 AWSs with a high rate of pressure change (≥2 hPa/10 min) during April 25–26, 2008.

Table 1
Details of tide gauges and AWSs presented in Fig. 1.

Type	Longitude (°E)	Latitude (°N)	Location
Tide gauge	126.3528	37.0075	DaeSan (DS)
	126.1323	36.6737	AnHeung (AH)
	126.4861	36.4064	BoRyeong (BR)
	126.5631	35.9755	GunSan (GS)
	126.3017	35.6181	WiDo (WD)
	126.4207	35.4262	YeongGwang (YG)
	125.4356	34.6842	DaeHeuksando (DH)
	126.3001	33.9618	ChuJado (CJ)
	126.5432	33.5275	JeJu (JJ)
	126.2512	33.2143	MoSeulpo (MS)
AWS	126.7507	37.4722	BuPyeong (BP)
	126.1684	36.9587	AnDo (AD)
	126.3167	36.5333	AnMyon (AM)
	126.9208	36.2724	BuYeo (BY)
	126.3153	35.8584	MalDo (MD)
	126.6970	35.4266	GoChang (GC)
	126.4778	35.2837	YeongGwang (YG)
	126.6042	35.2518	SangMudae (SM)
	126.3834	35.1993	YeomSan (YS)
	126.8813	35.1316	PungAm (PA)
	126.5264	35.0602	HamPyeong (HP)
	126.9843	35.0568	HwaSun (HS)
	126.7440	35.0250	NaJu (NJ)
	126.8278	34.9474	DaDo (DD)
	126.2933	34.8764	APheado (AP)
	126.3812	34.8169	MokPo (MP)
	126.1446	34.7269	AnJwa (AJ)
	125.4510	34.6872	DaeHeuksando (DH)
	126.5690	34.5535	HaeNam (HN)
	126.2394	34.5319	SuYu (SY)
	126.3238	34.4721	JinDo (JD)
	126.5000	33.5167	JeJu (JJ)
	126.1628	33.2938	KoSan (KS)

the wavelet analysis, a high common energy and phase relationship between the WPS of the two variables $XWPS(n,s)$ can be derived.

3. Results

3.1. Meteotsunami-induced harbor seiches

The sea level and meteotsunami records from six tide gauges at which the largest meteotsunami amplitude is observed are shown in Fig. 2. When the amplitude of high-frequency residual sea level components in the tsunami-frequency band (<2 h) exceeded 15 cm, it was then considered that a meteotsunami occurred at a tide gauge (Kim et al., 2021). On April 25–26, 2008, meteotsunamis were detected at seven tide gauges, specifically at the AH, WD, YG, DH, CJ, JJ, and MS. Sudden onset and rise in amplitude, followed by rapid dissipation (short-lived) in energy, were the primary characteristics of the observed signals in harbors. It is presumed that the meteotsunamis at the YG tide gauge lasted for a relatively long time as sequential tsunami-like sea level oscillations occurred. The YG tide gauge was located along a mound breakwater and inside the discharge canal of a nuclear power plant, which is vulnerable to the effects of topographic funneling.

The meteotsunami amplitude of each tide gauge was amplified with the respective maximum amplitudes at different arrival times, as shown in Fig. 2. From 21:00 to 23:00 KST on April 25, 2008, the maximum amplitudes were detected in tide gauges in the order of the AH, DH, WD, MS, YG, CJ, and JJ. Sequential meteotsunamis occurred in different tidal phases between the ebb tide, low tide, and flood tide, corresponding to low water levels. The ranges of the meteotsunami (30–60 cm) were approximately one order smaller than those of tides (2–6 m); however, their frequencies were approximately 25 times higher when comparing the sea level oscillations with a 30 min period and semidiurnal tides (Monserrat et al., 2006). Consequently, meteotsunami currents can be 2.5 times stronger than tidal currents and can cause severe damage. On March 31, 2007, May 4, 2008, and April 26, 2011, as mentioned above, loss of life and severe damage to property were reported due to the destructive meteotsunamis in the Yellow Sea (Kim et al., 2019). Although the meteotsunamis without any warning occurred at the time, no accident records were reported. Overall, the meteotsunami event on April 25, 2008, exhibited similar characteristics of sea level variability to the reported meteotsunami events: (i) localized peaks in the tsunami-frequency band and non-periodic signals due to energy generation and dissipation; (ii) strong meteotsunami amplitudes, particularly at harbor tide gauges; and (iii) occurrence of sequential meteotsunamis at multiple tide gauges.

The amplification patterns of the meteotsunamis propagating to multiple harbors as non-stationary signals in the time domain can be examined using the wavelet transform. The WPS of sea level at the AH, WD, YG, DH, CJ, and MS tide gauges for the meteotsunami event are shown in Fig. 3. We identified the period bands in which the largest amplification occurred by comparing the WPS of each period band before and after the meteotsunami event. The ranges of the WPS at diurnal and semidiurnal tidal periods depended on the location of the tide gauges, and they were found to be 10^2–10^4 and 10^3–10^5 cm^2min,

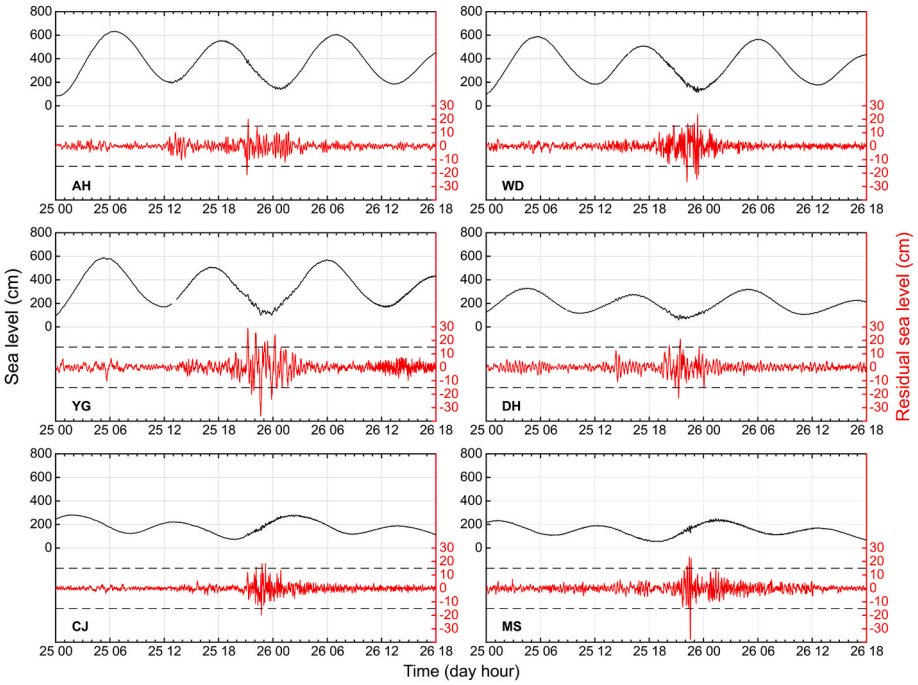


Fig. 2. Sea level (black lines) and 2 h high-pass filtered residual sea level (red lines) from the AH, WD, YG, DH, CJ, and MS tide gauges during 25–26 April 2008. The black dashed lines represent the meteotsunami amplitude limit of 15 cm.

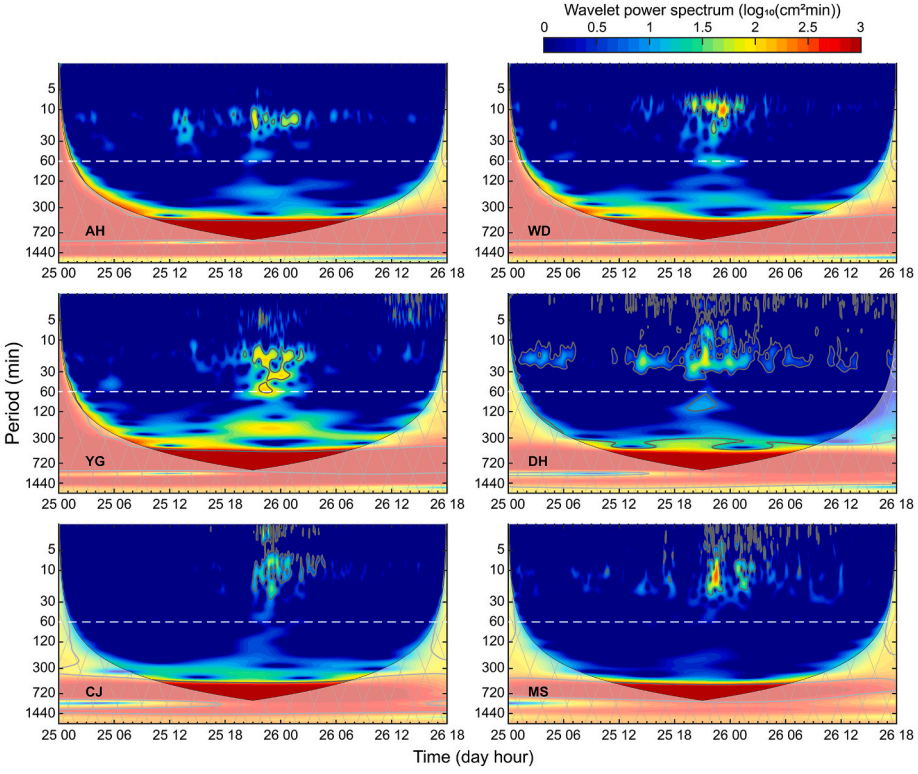


Fig. 3. Wavelet power spectrum (WPS) for the sea level. The y-axis represents the Fourier period (min). The thick gray lines enclose regions of 5% significance level for the corresponding red-noise spectrum during 42 h. The shaded and cross-hatched areas cover the cones of influence in which data are less reliable. The white dashed lines highlight the period bands of less than 1 h, where the maximum energy increases occurred compared to before the meteotsunami event.

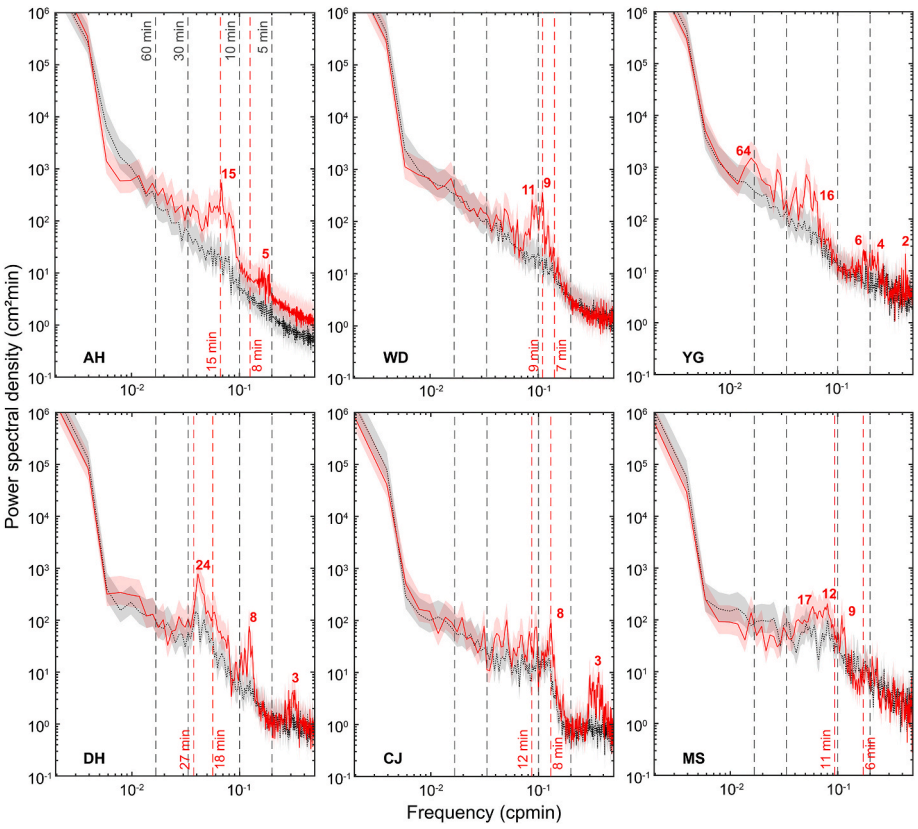


Fig. 4. Comparison of power spectral density in the residual sea level. The red lines and the black dashed lines indicate background noise of less than 1 h during the meteotsunami period (days 25–27) and calm period (days 23–25), respectively. The 95% confidence intervals are shown as the shaded areas. The period bands of the pronounced spectral peaks (min) are indicated. The distance of the red dashed lines is the range of the estimated fundamental period (min).

respectively, which were almost the same before and after the meteotsunami event. However, the WPS increased by up to two orders of magnitude in the period bands of less than 5 h from 18:00 to 03:00 KST on April 25–26, 2008. In particular, significant WPS increases were observed in the period bands of less than 1 h, as indicated by the white dashed lines in Fig. 3. This was primarily observed at the AH, WD, DH, CJ, and MS tide gauges located in the harbors and at the YG tide gauge located along the breakwater. In the background noise of less than 1 h, the amplification of different WPS levels was dominant in each resonance period band during the meteotsunami event (Monserrat et al., 2006). The amplification was not localized within the period bands of less than 1 h but extended over a range of 1–5 h (Šepić et al., 2012).

The power spectral density of a calm period and the meteotsunami period were compared through spectral analysis (Pattiaratchi and Wijeratne, 2009) to identify the distribution of the amplified spectral energy in the background noise of less than 1 h (Fig. 4). The spectral analysis of 2 days of the residual sea level was performed before the meteotsunami period of April 23–25, 2008, and during the meteotsunami period of April 25–27, 2008. The spectra of the sea level data were estimated using the Welch method, along with 95% statistical confidence intervals (Thomson and Emery, 2014; Welch, 1967). We used a Hamming window with half-window overlaps to improve the spectral estimates. The length of the window was selected to be 512 min, yielding ten degrees of freedom per spectral estimate for each period. Based on the spectral analysis, the characteristics of the spectral energy distribution during the meteotsunami period are as follows: (i) significant increases in the spectral energy occurred in the period bands ranging from 5 to 30 min at the AH, WD, and DH tide gauges; (ii) the spectral energy at the CJ and MS tide gauges increased slightly in the spectral peaks of less than 30 min without any dominant spectral peak; and (iii) the main changes in the spectral energy at the YG tide gauge were distributed in relatively long-period bands (16–60 min). The differences in the distribution of the spectral energy between the tide gauges are presumably related to the influence of local topography (Rabinovich, 2009).

We measured the similarity between the period bands of the pronounced spectral peaks and the analytical fundamental period of semi-closed harbors calculated using the modified Merian's formula (Rabinovich, 2009; Wilson, 1972). Based on the assumption that each harbor has a rectangular basin with a linear depth profile, the fundamental period (T_0) can be estimated using Eq. (3):

$$T_0 = 2.618\frac{2L}{\sqrt{gh}} \tag{3}$$

where L is the basin length, g is the acceleration due to gravity, and h is the depth of the harbor entrance. The depth range near the entrance was used to calculate the fundamental period of the basin. This is because the depth value of each harbor entrance showed a wide range. As indicated

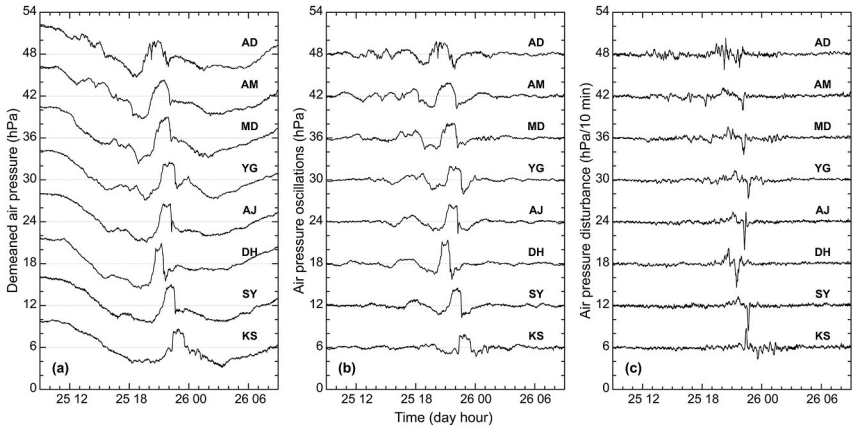


Fig. 5. Air pressure of the AD, AM, MD, YG, AJ, DH, SY, and KS AWSs during days 25–26 within the meteotsunami event: (a) demeaned air pressure, (b) air pressure oscillations (5 h high-pass filtered air pressure), and (c) air pressure disturbances (rate of raw pressure data changes over 10 min).

by the red dashed lines in Fig. 4, the ranges of the estimated fundamental periods of the AH, WD, DH, CJ, and MS harbor tide gauges were 8–15, 7–9, 18–27, 8–12, and 6–11 min, respectively, except for the YG tide gauge located in the breakwater. In particular, each range of the fundamental period at the AH, DH, and WD tide gauges corresponded to the period bands of the pronounced spectral peaks. The similarity between the resonance period bands from the spectral analysis and the fundamental periods at multiple harbor tide gauges revealed that there were meteotsunami-induced harbor seiches. We found a discrepancy between the period bands at the MS harbor tide gauge. The exact fundamental period could not be calculated using Merian's formula for semi-closed basins of simple geometric shapes, as the MS tide gauge was located in the harbor with complex geometric shapes. The resonant spectral energy in the broad period bands containing each fundamental period increased by one order of magnitude relative to the background noise spectral energy. This result is consistent with the established fact that dominant period bands of the observed harbor seiches are primarily related to the resonance characteristics of the local topography (Rabinovich, 2009).

3.2. Atmospheric disturbances associated with a squall line passage

As shown in Fig. 5, significant oscillations were also observed in the air pressure when large amplitude seiches were detected at the harbor tide gauges. At the eight outer-located AWSs from the coast, high-frequency air pressure oscillations superposed on the low-pressure system were observed in the demeaned air pressure time series (Fig. 5a). The pressure data were 5 h high-pass filtered to obtain the air pressure oscillations (Fig. 5b). The range of the air pressure oscillations recorded at the DH AWS during the meteotsunami event was sufficiently large to be close to the daily ranges of air pressure (6–8 hPa). These air pressure oscillations were observed on a spatial scale of at least 400 km across the eastern Yellow Sea coast in the north-south direction from the BP AWS to KS AWS (Fig. 1). In particular, more pronounced box-like air pressure oscillations were widely detected at the AJ, DH, and SY AWSs located in the southern region of Korea. It is presumed that the air pressure oscillations recorded at multiple AWSs were related to the propagation of the meteotsunamis because they have similar timing of occurrence and spatial scale.

To estimate the intensity of the pressure-forced meteotsunamis, an air pressure disturbance indicating a steep slope for a short time was calculated from the raw pressure data. The intensity of the air pressure oscillation can be estimated as a range of high-frequency pressure. However, it is challenging to directly assess whether the air pressure oscillations can generate significant sea level oscillations. A rapid change in air pressure of 2–4 hPa over a few minutes can typically generate high-frequency and tsunami-like sea level oscillations that are dominant in the period bands ranging from a few minutes to a few hours (Hibiya and Kajiura, 1982; Jansà et al., 2007; Rabinovich et al., 2021; Šepić et al., 2009a, 2012). The air pressure disturbance considered in this study was the rate of the raw pressure data change over 10 min (Fig. 5c). In the reported meteotsunami events of the Yellow Sea, air pressure disturbances of 1.7–4.8 hPa/10 min were commonly observed at multiple AWSs (Kim et al., 2019). On April 25, 2008, significant air pressure disturbances above 2 hPa/10 min, which exceeded the minimum intensity of the air pressure disturbances observed in the reported events, were recorded at at the coastal 23 AWSs (Fig. 1). The air pressure disturbances of the negative peak occurred with a considerably sharper rate of pressure changes than those of the positive peak at most AWSs. In particular, there seems to be a link between the strongest air pressure disturbances of 3.4–4.0 hPa/10 min recorded at multiple AWSs in the southern region and relatively strong meteotsunamis recorded at the YG, DH, and MS tide gauges along the southern coast of Korea.

Interestingly, wind shifts were observed only at the AD, MD, DH, and KS AWSs installed on islands off the eastern Yellow Sea coast (Fig. 6) when the air pressure oscillations and disturbances were observed at multiple AWSs (Fig. 5b and c). The magnitude of wind speed observed at most AWSs located along the coast and in inland areas was less than 10 m/s. Temporal variations in the along- and cross-shore wind were compared to determine the possible causes of the wind shifts. Before the wind shifts were detected at the AWSs, the south wind was predominant at approximately 10–20 m/s owing to the low-pressure system, and the cross-shore wind was recorded to be less than 5 m/s. However, the wind shifts occurred as the cross-shore wind reached a maximum of 10–16 m/s. The wind shifts were observed in the period of the air pressure oscillations, as indicated by the black dashed lines and gray shaded areas in Fig. 6. After the wind shifts, the wind pattern recovered to the same level as before the occurrence of the wind shifts. Meteorological

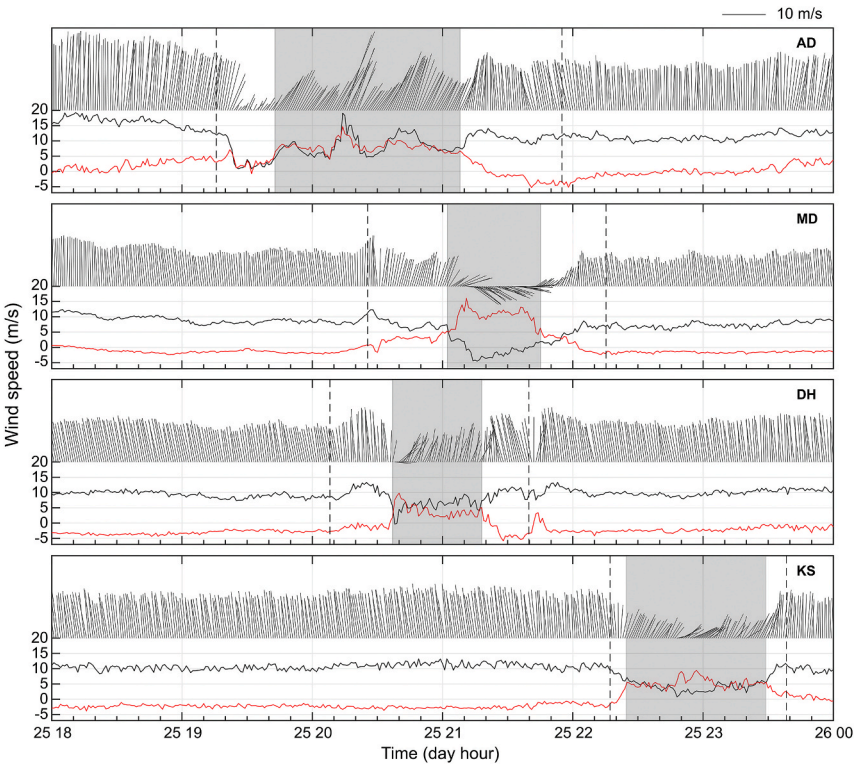


Fig. 6. Wind variations at the outer-located AD, MD, DH, and KS AWSs on day 25 within the meteotsunami event. The black and red lines denote along- (north and southward) and cross-shore (east and westward) wind, respectively. The gray shaded areas highlight the wind shifts due to the rapid cross-shore wind above 5 m/s. The durations of the box-like air pressure oscillations are shown as the black dashed lines (see Fig. 5b).

parameters such as air pressure oscillation, air pressure disturbance, and wind shifts suggest the passage of a squall line (Churchill et al., 1995; Kazeminezhad et al., 2021; Šepić and Rabinovich, 2014; Tepper, 1950).

The evolution of the squall line was traced by a box-like air pressure oscillation. Air pressure oscillation is one of the meteorological parameters indicating a physical mechanism of the squall line (Tepper, 1950). Based on the SAWP (i.e., weighted sum of WPS) of the air pressure oscillations at multiple AWSs, the temporal and spatial variability of the squall line can be expressed as a power Hovmöller diagram, which provides a measure of the wavelet variance for air pressure oscillations at each time and longitude, as shown in Fig. 7a. The maximum SAWP of 2.7 hPa^2 was observed at the DH AWS among all AWSs. The SAWP above 50% of the maximum SAWP (1.35 hPa^2) was assumed to be the core of the squall line. The core, shown as orange to red contours in Fig. 7a, was traced over the longitudes and times. Consequently, the core that was moving eastward disappeared rapidly in the longitude bands between 126.5°E and 127°E, approximately 100 km away from the DH AWS.

To further examine the duration and dissipation pattern of the squall line in the Yellow Sea, the power Hovmöller diagram of the air pressure oscillations was averaged over all longitudes and all times (Fig. 7b and c). The average SAWP over all longitudes is represented as a Gaussian-like distribution (Fig. 7b). The duration of the squall line can be estimated from the full duration at half maximum of the distribution. The duration was from 18:18 to 00:49 KST on April 25–26, 2008, which was similar to the time when the meteotsunami amplitudes were continuously detected in multiple tide gauges (Fig. 2). In particular, the maximum meteotsunami amplitudes were intensively detected at most tide gauges around the time when the maximum intensity of the squall line appeared at 21:27 KST on April 25, 2008 (Fig. 7b). Since then, the intensity of the squall line moving toward the eastern Yellow Sea coast was not constant but decreased with time and space (Fig. 7a). The squall line of the maximum intensity (P_{max}) recorded at the DH AWS decreased exponentially as it propagated toward the coast (Fig. 7c). The longitudinal distribution of power was then reduced by half (P_{half}) near 126.8°E, where the core of the squall line also disappeared. Finally, it quickly dissipated in the inland areas of Korea. Therefore, we identified a similar phase relationship between the squall line and meteotsunamis before the squall line dissipation phase, and there were no forces other than the squall line during the meteotsunami event.

3.3. Link between atmospheric disturbances and meteotsunamis

We considered the meteotsunami event on April 25, 2008, as a pressure-induced event. Strong air pressure disturbances exceeding 2 hPa/10 min were detected at the 23 AWSs located along the eastern Yellow Sea coast. However, the maximum wind speed above 10 m/s was detected only at the 4 AWSs. To examine the correlation between the squall line and meteotsunamis exhibiting a similar phase relationship, the time series of the air pressure and sea level oscillations (5 h high-pass filtered) observed at the DH harbor were compared (Fig. 8a and b). Among the 126 AWSs and 10 tide gauges in the Yellow Sea, the DH AWS and tide gauge have the following implications: (i) a unique observation point where the pressure and sea level data sets were recorded with the same space and the nearest distance; (ii) the observation point where the

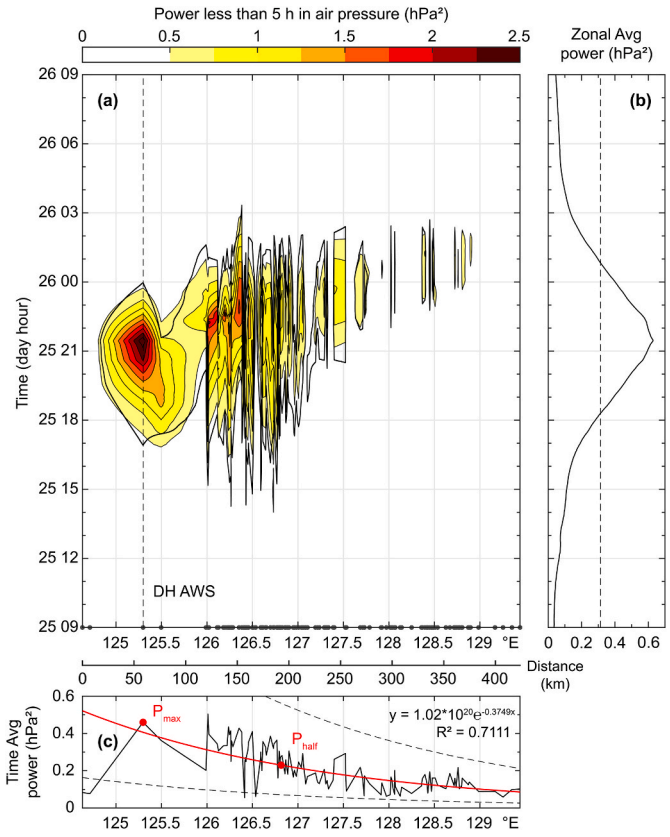


Fig. 7. Evolution of the air pressure oscillations derived from all AWSs. (a) Power Hovmöller diagram of less than 5 h scale-averaged wavelet power (SAWP) in air pressure. The SAWP time series at each longitude is linearly interpolated. The black dots on the bottom of the x-axis represent the locations of the 126 AWSs. The color contour interval is 0.25 hPa^2. The thick black contours represent the 5% significance level against the corresponding red noise spectrum at each AWS. The black dashed line indicates the DH AWS with the maximum SAWP detected in the Eastern Yellow Sea. (b) Average SAWP over all longitudes. The duration of the air pressure oscillations was estimated as full duration at half maximum, which is shown as the black dashed line. (c) Average SAWP over all times. The red line represents the rapid dissipation of the air pressure oscillations along the longitudes estimated using exponential regression, and the black dashed lines represent the 95% confidence intervals for the regression.

strongest intensity of the air pressure oscillation and disturbance was detected on April 25, 2008; and (iii) the outer-located observation point where air pressure disturbances were always detected in the previously reported events, which is ideal for monitoring the pressure-forced meteotsunamis (Kim et al., 2019). Similar to a sign-inverted waveform, as shown in Fig. 8a and b, the wave envelope of the sea level oscillations was locked to the box-like air pressure oscillations, which have broad period bands. The coupled mode provides strong evidence that the link between the air pressure and sea level oscillations might have lasted from the open sea to the DH harbor. When the Froude number (F_r), which is the speed ratio between air pressure oscillations and resultant long ocean waves, is approximately 1.0 in the open sea, sea level oscillations of up to several tens of centimeters can be produced by the dynamic sea level response (Proudman, 1929).

The cross-wavelet transform was performed to analyze the linked period band between the air pressure and sea level oscillations (Fig. 8c). When estimating the correlation between two non-stationary signals, it is possible to calculate the covariance of the WPS at a specific time and period through the cross-wavelet transform of the normalized time series (Torrence and Compo, 1998). The two signals co-vary with the highest energy around the 110 min and 220 min period bands from 18:00 to 00:00 KST on April 25–26, 2008. Similar to the coupled mode of the inverted waveform (Fig. 8a and b), the arrows show anti-phase relationships in the corresponding period bands (Fig. 8c). A phase relationship with almost no time delay was observed in the 110 min period band. Evidently, the locked wave packet was generated by the dynamic reaction of the air pressure oscillations centered at the 110 min and 220 min period bands. This result is based on the coupled mode of the air pressure and sea level oscillations in the time domain and the highest common energy between the two signals with the anti-phase in the wavelet domain.

The period bands where the air pressure and sea level oscillations were highly correlated (Fig. 8c) and the dominant period bands of the meteotsunamis (Fig. 4) were different at the DH harbor. Another significant common energy was observed with the inconsistent phase relationship at 8 min and 24 min period bands, which are the resonance period bands of the harbor (Fig. 4). As respective standard deviations normalize XWPS, it can be considered a type of covariance between two WPS (Grinsted et al., 2004; Torrence and Compo, 1998). A significant XWPS can be derived when a specific variable exhibits a relatively high WPS. Thus, the high XWPS at 8 min and 24 min period bands was associated with the WPS of sea level oscillations, which have dominant energy around the first and fundamental mode periods of the DH harbor, unlike the WPS of the air pressure oscillations. During the meteotsunami event, there was additional amplification at the resonance period bands of the DH harbor after the amplification at 110 min and 220 min period bands due to the coupled-mode propagation of the air pressure and sea level oscillations. In other words, the categorization of the resonance period bands shows that forced oscillations occurred (Rabinovich, 2009), indicating that the dominant period of the external forcing differs from that of the basin (Garcies et al., 1996; Gomis et al., 1993; Wilson, 1972).

Monserrat et al. (2006) stated that the propagation (speed and direction) of the atmospheric disturbances might be more important than the actual energy content of the forced long waves. As a first try, air pressure oscillation was used to track the energy evolution of the squall line (Fig. 7) and examine its relationship with the resultant meteotsunamis (Fig. 8). However, it was difficult to estimate the potential amplitude of pressure-forced meteotsunamis with air pressure oscillation. In general, significant sea level oscillations are likely to occur when the traveling air pressure disturbance exceeds 2 hPa/5–40 min (Šepić and Vilibić, 2011; Šepić et al., 2012). In the Yellow Sea, an air pressure disturbance monitoring system was operated based on the intensity and propagation of the air pressure disturbances detected in the reported meteotsunami events. According to the monitoring system, when air pressure disturbances over 1.2 hPa for 10 min (0.12 hPa/min) propagated to multiple AWSs, meteotsunami amplitudes over 10–15 cm were likely to be detected (Kim et al., 2019, 2021). In this study, we considered a rate of pressure change exceeding 2 hPa for 10 min as an air pressure disturbance (0.2 hPa/min) to track the propagation pattern of the strong air pressure disturbances favorable to meteotsunami occurrences. Then, it was possible to plot a propagation map (isochrone map)

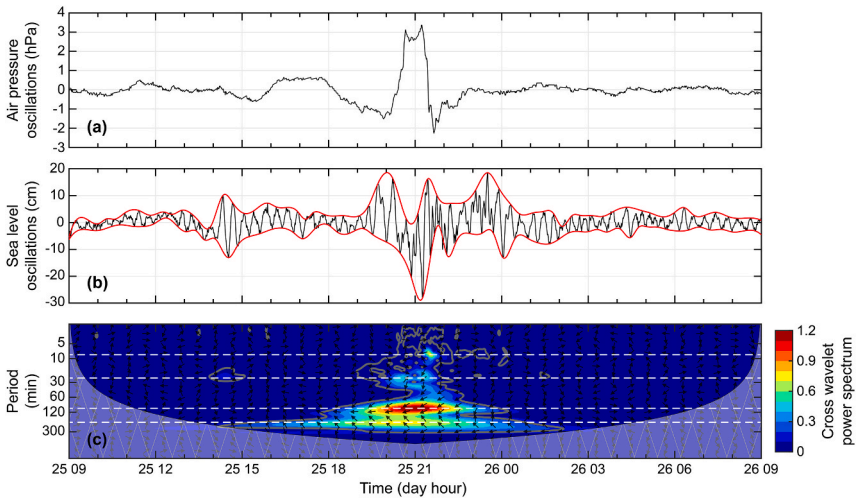


Fig. 8. Correlation between air pressure oscillations and resultant sea level oscillations in the time-frequency domain at the DH AWS and tide gauge. (a) 5 h high-pass filtered air pressure. (b) 5 h high-pass filtered sea level (black line) and its wave envelope (red line). (c) Cross-wavelet transform of the normalized air pressure and sea level oscillations. The thick gray contours represent the 5% significance level against red noise. The relative phase relationship is illustrated as arrows (with in-phase pointing right, anti-phase pointing left, and air pressure oscillations leading sea level oscillations by 90° pointing straight down). The shaded and cross-hatched areas indicate the cone of influence in which data are less reliable. The white dashed lines highlight their dominant period bands (8, 24, 110, and 220 min).

by utilizing the arrival times and positions of multiple AWSs where air pressure disturbances were detected (Fig. 9a).

The propagation patterns of air pressure disturbances and meteotsunamis are shown in Fig. 9 for the duration of the squall line in the Yellow Sea (Fig. 7b), from 18:18 to 00:49 KST on April 25–26, 2008. The arrival time at each tide gauge was determined as the time of the maximum peak with the meteotsunami amplitude exceeding 15 cm when estimating the propagation of the meteotsunamis. The propagation speed and direction of the meteotsunamis that vary temporally and spatially can be calculated even with limited tide gauges using a list of arrival times, location of the tide gauges, and long ocean wave speed (Kim et al., 2020). The air pressure disturbance initially traveled at a speed of approximately 11 m/s from the WNW direction and then rotated counterclockwise along the coastline before propagating rapidly at a speed of 19 m/s (Fig. 9a). The sequential arrival of the meteotsunamis in the order of the AH, DH, WD, MS, YG, CJ, and JJ tide gauges (Fig. 9b) revealed a similar propagation direction to the air pressure disturbances. However, the meteotsunamis propagated at an average speed of 22 m/s, which is faster than the average speed of the air pressure disturbances (15 m/s). Similar to the forced oscillations propagating toward the entrance of the DH harbor (Fig. 8), the air pressure disturbances and meteotsunamis also exhibited a pattern of coupled-mode propagation, which is shown as the isochrones in Fig. 9.

Based on the meteorological images of the atmospheric disturbances captured during the squall line passage, we can demonstrate the validity of the derived propagation patterns of the air pressure oscillations (Fig. 7), air pressure disturbances (Fig. 9a), and meteotsunamis (Fig. 9b). The spatially averaged power of the air pressure oscillations (Fig. 7b) and rain cluster (Fig. 10a) showed the highest intensity from 21:00 to 22:00 KST on April 25, 2008. As the isochrone of the air pressure disturbances at the time (Fig. 9a) corresponded to blank areas of the AWS, the air pressure disturbances were detected after 22:00 KST on April 25, 2008, primarily at the inland AWSs. Although the arrival time of each atmospheric disturbance was slightly different, the intensity distribution over time was coincident. The air pressure disturbances showed a high-intensity distribution in the 34–35°N latitude bands (Fig. 9a), in agreement with the intensity distribution of the rain cluster at 21:00 KST on April 25, 2008 (Fig. 10a). Similarly, rapid energy dissipation along the coastline during landing was also observed in air pressure oscillation (Fig. 7c), air pressure disturbance (Fig. 9a), rain rate (Fig. 10a), and lightning strike (Fig. 10b). The strong air pressure disturbances of at least 2.7 hPa/10 min spread locally to multiple AWSs near the DH, WD, MS, and YG tide gauges located in harbors or breakwaters. This implies that the passage of squall line was related to meteotsunami-induced harbor seiches in the south-central region of Korea. As the first pre-amplified oscillations forced by the squall line from the open sea were delivered to the entrance of the semi-closed basins, strong seiches occurred sequentially at each harbor and breakwater located along the propagation path of the high-intensity air pressure disturbances.

4. Discussion

4.1. Propagation and amplification

On April 25–26, 2008, a squall line traveled toward the west coast of Korea across the Yellow Sea, causing the propagation of 2–4 hPa/10 min intensity of air pressure disturbances at 23 AWSs. Finally, maximum meteotsunami amplitudes of 15–38 cm were detected at seven tide gauges. The Proudman resonance due to coupled-mode propagation can enhance the amplitude of sea level oscillations (Proudman, 1929). It is important to estimate the amplification due to the external resonance between atmospheric and long ocean waves in terms of potential meteotsunami prevention (Monserrat et al., 2006; Pattiaratchi and Wijeratne, 2015; Rabinovich, 2009). A simple linear equation was used to calculate the amplitude of the long ocean waves amplified during propagation by the traveled air pressure disturbance in the open sea (Hibiya and Kajiura, 1982):

$$\zeta_P = \frac{\zeta_0}{L}\frac{x_f}{2} \tag{4}$$

where ζ_P is the amplified amplitude under the condition of the Proudman resonance, ζ_0 is the inverted barometer response of sea level, L is the spatial scale of the air pressure disturbance, and x_f is the distance

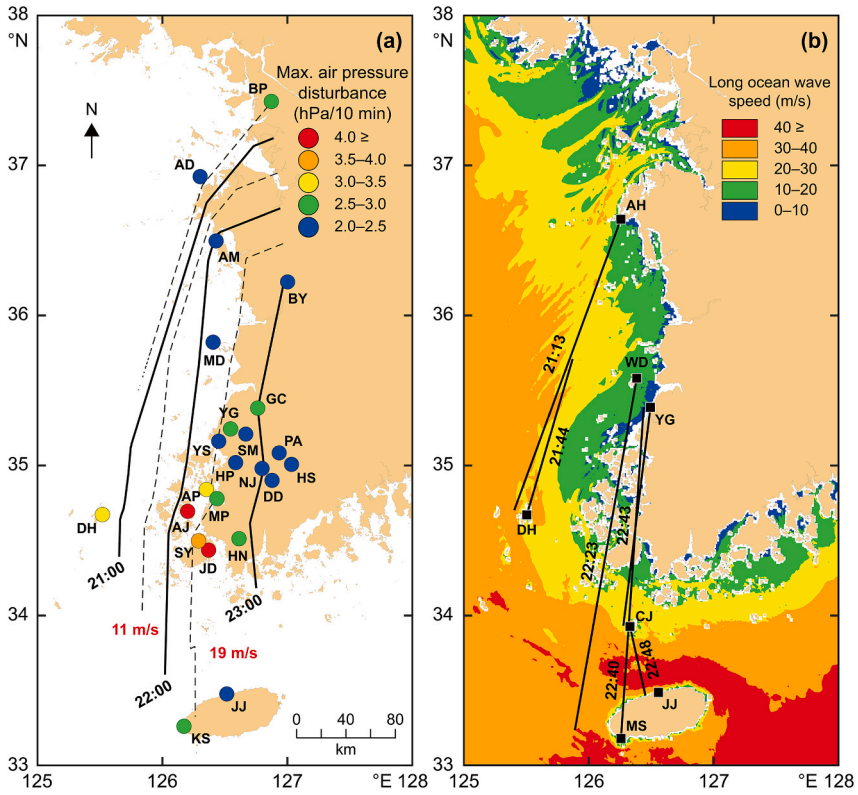


Fig. 9. Propagation of air pressure disturbances (rate of pressure changes over 10 min) and meteotsunamis from 18:18 to 00:49 KST on April 25–26, 2008. (a) Circles mark the 23 AWSs where the air pressure disturbances exceeded 2 hPa/10 min. The colors of circles denote the intensity of the maximum air pressure disturbance during the squall line passage. The thick black lines and black dashed lines indicate isochrones of the air pressure disturbance (1 h and 30 min) calculated from the arrival time list and locations of each AWS, respectively. (b) Colors on the map show the long ocean wave speed of the eastern Yellow Sea. The black squares mark tide gauges where the meteotsunamis arrived. The thick black lines indicate the isochrones of the meteotsunamis in the order of arrival time.

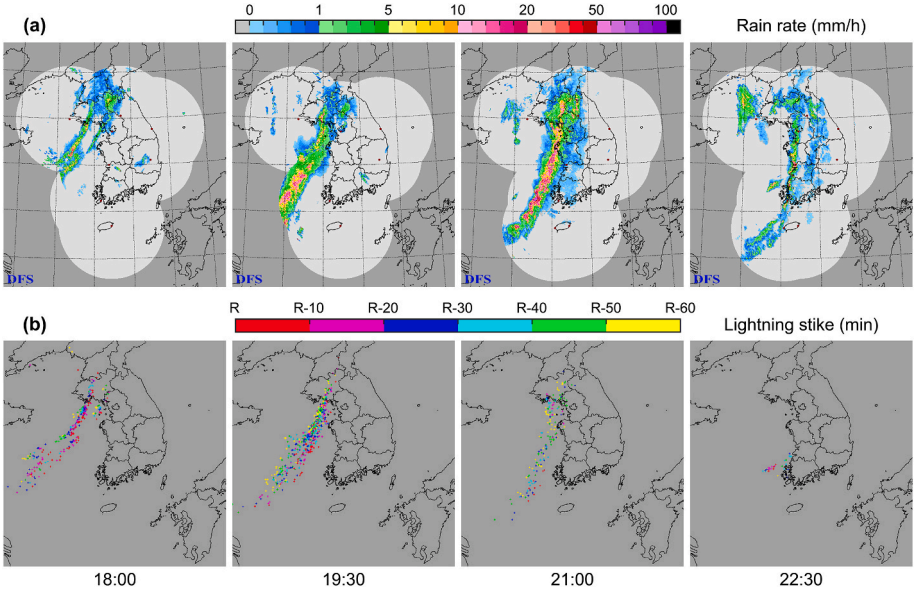


Fig. 10. Meteorological images of the atmospheric disturbances from 18:00 to 22:30 KST on April 25, 2008: (a) rain rate on radar images and (b) temporal distribution of lightning strike (Note: R is reference time). The images were downloaded from https://www.kma.go.kr/eng/weather/images/radar.jsp.

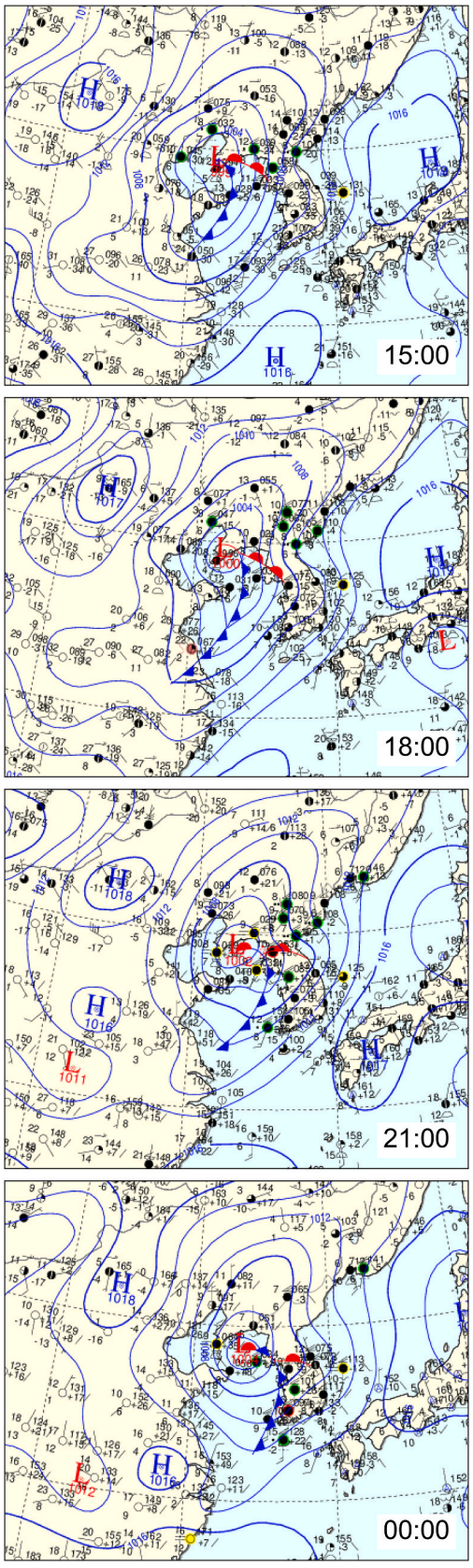


Fig. 11. Surface pressure charts illustrated every 3 h from 15:00 to 00:00 KST on April 25–26, 2008. The images were provided by the Korea Meteorological Administration (KMA).

traveled from the source location.

The source location and propagation path of the air pressure disturbance can be obtained from 3 h interval surface pressure charts (Fig. 11). In the pressure charts, the center of the low-pressure system was located in the middle of the Shandong, Liaodong, and Ongjin Peninsulas. The squall line and cold front propagated across the isobars from the Shandong Peninsula along the eastern Yellow Sea coast. The cold front (Fig. 11) was located behind or almost along with the linear cluster of the lightning strike (Fig. 10b) at 21:00 KST on April 25, 2008. Generally, a squall line is a line of thunderstorms that form simultaneously and ahead of a cold front (Tepper, 1950). The source location of the squall line and its propagation can be tracked based on the cold front in the pressure charts. ζ_P was calculated for the DH tide gauge, the outer-located observation point near the open sea. Thus, x_f was determined as the arc distance of the cold front near the Shandong Peninsula to the entrance of the DH harbor ($x_f = 439$ km). However, as it is impossible to determine from which point the coupled mode was originated, the estimated amplitude can be overestimated. L was derived ($L = Ut$) using the average speed of the squall line ($U = 13.6$ m/s) based on the surface pressure charts and the elapsed time ($t = 44$ min) from the trough (19:55 KST) to the peak (20:39 KST) of the air pressure oscillation at the DH AWS (Fig. 8a). When we assume that ζ_0 is determined as the corresponding inverted barometer response at the arrival time of the air pressure disturbance ($\zeta_0 = 2.2$ cm), ζ_P in front of the entrance of the DH harbor can be theoretically amplified up to 13.4 cm. The dynamic sea level response due to the propagation with the air pressure disturbance in the open sea was estimated to approximate the meteotsunami amplitude limit in the Yellow Sea. The estimated ζ_P/ζ_0 was approximately 6, which was overestimated compared to the ratio (4–5) suggested by Monserrat et al. (2006).

There is coastal amplification (e.g., shoaling at the shelf, narrowing at the harbor entrance, and reflection) in the nearshore wave transformation stage in addition to amplification at the open sea propagation stage. Accordingly, the observed meteotsunami amplitudes can be affected by other amplification or dissipation mechanisms, such as shelf amplification (Garcies et al., 1996; Gomis et al., 1993; Wilson, 1972), wave-current interaction (Linares et al., 2019), and infragravity period (20–300 s) oscillations (Okihiro et al., 1993; Thotagamuwage and Pattiaratchi, 2014). Based on the above-mentioned process, Orlić et al. (2010) estimated the amplification during the propagation of meteotsunami. However, there can be significant errors when estimating the amplification factor using only coastal tide gauge data. Another approach is using the generation coefficient suggested by Šepić and Rabinovich (2014) to make the amplification more visible at each observation point:

$$G^j_{max} = \frac{\zeta^j_{max}}{\zeta^j_0} \tag{5}$$

where G^j_{max} is the generation coefficient at *the* j-th tide gauge, ζ^j_{max} is the maximum amplitude of the meteotsunamis, and ζ^j_0 is the inverted barometer response derived from the maximum intensity of the air pressure disturbance arriving at the AWS near the tide gauge. The distributions of ζ_0, ζ_{max}, and ζ_{max}/ζ_0 at each tide gauge along the eastern Yellow Sea coast are shown in Fig. 12. As the observed meteotsunami amplitudes exceeded the estimated ζ_P (13.4 cm) and meteotsunami amplitude limit (15 cm) at the AH, WD, YG, DH, and MS tide gauges located in semi-closed basins, the generation coefficient increased by approximately an order of magnitude or higher. Similar to the reported meteotsunami events (Kim et al., 2019), the strong amplification at the YG tide gauge was likely due to the funnel effect along the breakwater in front of the tide gauge. A generation coefficient of less than 5 was calculated at the DS, BR, and GS tide gauges, where ζ_{max} was detected below the meteotsunami amplitude limit.

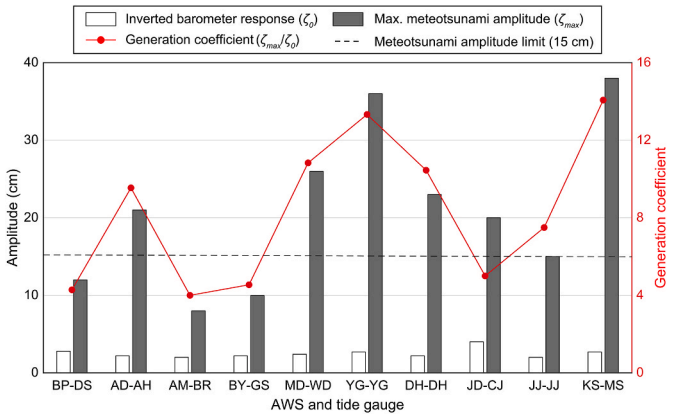


Fig. 12. Inverted barometer response, maximum meteotsunami amplitude, and generation coefficient (Šepić and Rabinovich, 2014) at each AWS and tide gauge (red line). The black dashed line indicates the meteotsunami amplitude limit in the Yellow Sea.

4.2. Local amplification in semi-closed basins

The energy content of the incoming long waves was examined to understand the significant amplification ($\zeta_{max}/\zeta_0 \geq 10^1$) observed primarily in the semi-closed basins. The spectral energy of the long ocean waves could not be directly identified before they arrived at the harbor entrance because the tide gauges were located on the coast or in semi-closed basins (Fig. 13). The sea level oscillations observed at the tide gauges included sea level response through the amplification and attenuation of the external forcing (arriving waves) by local topography. To eliminate the influence of topography and examine the source characteristics, we estimated the ratio between the spectra of the meteotsunami period and calm period (Monserrat et al., 1998; Rabinovich, 1997). The observed spectrum during the meteotsunami event (S_{obs}) as a function of frequency (f) may be presented as the sum of the energy generated by the atmospheric source (S_m) and the energy of the background surface oscillations (S_b):

$$S_{obs} = S_m(f) + S_b(f) \tag{6}$$

Based on the assumption of linear topographic responses for the inlets, which implies that they are not a function of amplitudes but a function of frequencies, then:

$$S_m(f) = A(f)E_m(f); S_b(f) = A(f)E_b(f) \tag{7}$$

where $A(f)$ is the amplification due to the resonance properties of the local topography, which is assumed to be constant in time, although strongly variable in space. $E_m(f)$ and $E_b(f)$ are related to external forcing (i.e., incoming long waves) during the event and background conditions, respectively. When the energy of the background surface oscillations is the same during the meteotsunami and calm periods, the spectral ratio, $R(f)$ can be expressed as follows:

$$R(f) = \frac{S_{obs}(f)}{S_b(f)} = \frac{E_m(f)}{E_b(f)} + 1 \tag{8}$$

The energy content of the incoming long waves during the event can be estimated using the spectral ratio, which is independent of the location of the tide gauges (Rabinovich and Stephenson, 2004).

The spectral ratios derived from the spectra of the meteotsunami period and calm period (Fig. 4) are shown in Fig. 14. The sea level oscillations of the six tide gauges were associated with the meteotsunamis that propagated from the open sea. Similar to the spectral analysis results (Fig. 4), local amplification centered on the resonance period band of each semi-closed basin was dominant due to harbor resonances. With the different amplification patterns, the dominant period bands of the amplification were 16–60 min at the YG tide gauge (breakwater). In addition, strong amplification of sea level oscillations of less than 5 min (i.e., infragravity waves) occurred at the YG, DH, and CJ tide gauges located in the southern region of Korea. The presence of a high-frequency source is related to the nonlinear interaction of wind waves

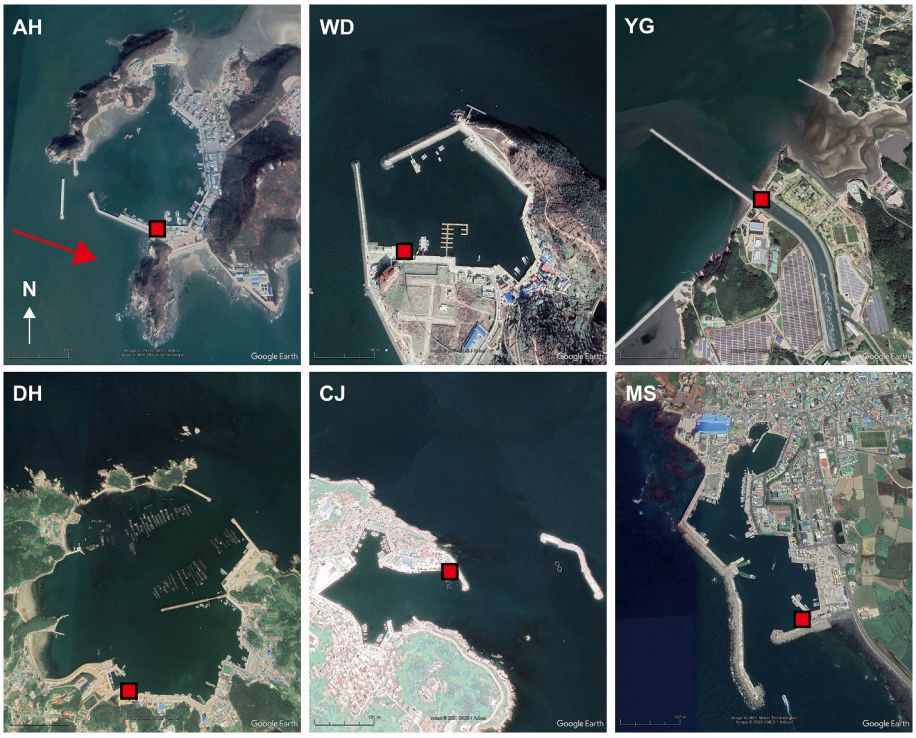


Fig. 13. Google Earth satellite images of the semi-closed basins in which the tide gauges (red squares) are located. The red vector shows the propagation direction of the air pressure disturbances and meteotsunamis (see Fig. 9).

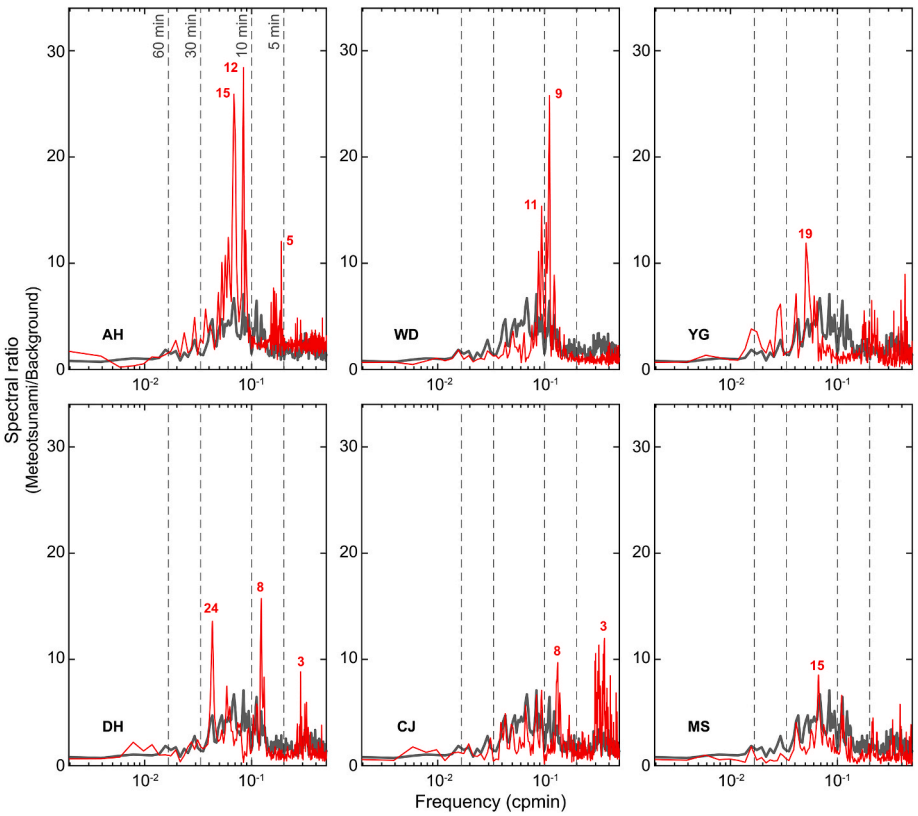


Fig. 14. Spectral ratios (red line), meteotsunami (days 25–27)/background (days 23–25), of the residual sea level (see Fig. 4). The dominant period bands of spectral peaks (min) are indicated. The thick gray line represents the average of the spectral ratios at the tide gauges.

(Oltman-Shey and Guza, 1987). The average of the spectral ratios (Marcos et al., 2009) can be considered as the spectral content of the long waves propagated toward the entrance of multiple harbors and caused sequential harbor seiches. As mentioned above, the dynamic reaction of the pressure-forced long waves from a certain source location in the open sea propagated toward each tide gauge in the semi-closed basin (Fig. 9). Based on the spectral ratios of the harbor tide gauges, the energy content of the incoming long waves was found to be concentrated in period bands of less than 30 min (Fig. 14). This means that the resonance period bands of the long waves generated harbor resonances at multiple harbors along the propagation path of the air pressure oscillations and disturbances.

The geometric features of the basin where each tide gauge was located were identified to investigate the resonance characteristics of the basins where the incoming long wave-induced amplification was observed. The geometric features were divided into basin type, entrance direction, length, and width (Table 2). Generally, the predominant direction of the incident wave toward the entrance direction is a favorable condition for additional amplification in a harbor and breakwater. Direct propagation of the air pressure disturbances and long waves along the breakwater or through the harbor entrance, as shown in Fig. 13, could result in amplification at the YG or AH tide gauge due to the funnel effect or harbor oscillations (Table 2). As the direction alone could not explain the amplification that also occurred in the other tide gauges, we attempted to determine the common amplification features using a quality factor (Q-factor). The Q-factor, which is a linear measure of the energy damping in a basin, can simply be estimated from the aspect ratio between the length and width of the harbor (Rabinovich, 2009). Consequently, significant generation coefficients were commonly found at the AH, WD, DH, and MS tide gauges, located in harbors with Q-factors above 6. A large Q-factor as a geometric feature for the amplification in each harbor is important when there is resonance matching between the dominant period of arriving waves and the eigen (resonant) period of the harbor (Monserrat et al., 2006).

4.3. Double resonance effect

A squall line and the resultant meteotsunamis were propagated in the coupled mode throughout the Yellow Sea, delivering the long ocean waves amplified during the propagation stage toward the AH, WD, DH, and MS harbors with large Q-factors. The resonance period bands of the incoming long waves to the harbor entrances have a wide eigen-period

Table 2
Geometric features of basins with the tide gauges installed in the harbor and breakwater.

Tide gauge	Basin type	Entrance direction[a] (°)	Length (m)	Width (m)	Q-factor (Length/Width)	Generation coefficient (ζ_{max}/ζ_0)
AH	Harbor	246	923	141	7	10
WD	Harbor	355	547	73	7	11
YG	Breakwater	303	1170	90	13	13
DH	Harbor	48	1750	208	8	10
CJ	Harbor	105	607	218	3	5
MS	Harbor	165	644	101	6	14

[a] Entrance direction is measured clockwise from the northward direction.

range of less than 30 min, which can generate harbor resonances in multiple harbors along the eastern Yellow Sea coast. The local amplification centered on the eigen period of each harbor sequentially occurred at the harbors on the propagation path of the air pressure disturbances. Consequently, it caused significant seiches in multiple harbors. The sequential amplification is defined as a double resonance effect, which is a combination of the Proudman resonance and harbor resonance (Monserrat et al., 2006; Rabinovich, 2009). Therefore, the seiches that occurred in the four harbors on April 25, 2008, were meteotsunami-induced harbor seiches. Similarly, strong seiches were reported in the DH harbor on March 31, 2007, with a maximum wave height of approximately 1 m due to the double resonance effect (Kim et al., 2016, 2019).

Monitoring the meteotsunami-induced harbor seiches has wider implications based on the common resonance characteristics of the double resonance effect. In this study, favorable conditions for the generation of the double resonance effect were identified as follows: (i) propagation of strong air pressure disturbance toward the harbors, (ii) the dominant period bands of the long ocean waves pre-amplified in the open sea; and (iii) harbors with large Q-factors. Every spring season (March to April) on the west coast of Korea, a pressure-forced meteotsunami warning system utilizing 89 land-based AWSs is operated in real-time (Kim et al., 2021). It is a potential meteotsunami warning system that can send alarm messages to mobile devices by monitoring the intensity and propagation path of air pressure disturbances. The meteotsunami-induced harbor seiches can also be monitored before the propagation of resonant waves to harbors with large Q-factors by applying the guidelines of the resonance characteristics to the current monitoring system. However, the dominant period bands of long ocean waves cannot be directly monitored in the monitoring system. Real-time monitoring of pre-amplified resonant waves remains challenging (Dusek et al., 2019). This is because buoy observations need to be performed at 1 min intervals identical to current sea level observations in tide gauges and preparing multiple buoys in the open sea to detect the resonance period bands of the long ocean waves propagated from each direction of the Yellow Sea. To supplement the current monitoring system, tracking the dominant period bands of the long ocean waves amplified by the Proudman resonance through numerical modeling is expected. Finally, it will be possible to provide a timely warning for the harbor seiches before pre-amplified waves propagate to harbors with large Q-factors by utilizing the monitoring system and prediction system.

5. Summary and conclusions

This study demonstrated the propagation and amplification process of meteotsunami-induced harbor seiches along the eastern Yellow Sea coast on April 25–26, 2008. Accompanied by the meteotsunami event, evidence of the squall line, such as air pressure oscillations, air pressure disturbances, wind disturbances, and a linear cluster of rain rate and lightning strike, was recorded in the majority of AWSs and meteorological images. The air pressure oscillations and resultant sea level oscillations were highly correlated in the time-frequency domain, and the air pressure disturbances propagated with the long ocean waves toward the west coast of Korea across the Yellow Sea. Consequently, the long ocean waves forced by the squall line generated meteotsunami-induced harbor seiches (i.e., double resonance effect) that caused sequential harbor resonances along the propagation path.

The common resonance characteristics of the double resonance effect in the Yellow Sea were as follows:

- The high rates of pressure changes above 2.7 hPa/10 min were detected near the harbor tide gauges located on the propagation path of the air pressure disturbances.
- The dominant period of the incoming long ocean waves pre-amplified by the Proudman resonance was estimated to be less than 30 min, which spanned the fundamental periods of harbors.
- The tide gauges were located in semi-closed basins with Q-factors above 6.

These results further suggest that the potential double resonance effect in harbors can be monitored based on the resonance characteristics. In conclusion, we can detect in advance whether the propagation of high-intensity air pressure disturbances is directed toward harbors with large Q-factors using the air pressure disturbance monitoring system in the Yellow Sea. However, it is challenging to monitor the dominant period bands of long ocean waves in real-time before entering each harbor. Therefore, it is necessary to supplement the current monitoring system through an atmosphere-ocean coupled model in the future.

Declaration of competing interest

The authors declare that they have no known competing financial interests or personal relationships that could have appeared to influence the work reported in this paper.

Acknowledgements

This research was supported by Basic Science Research Program through the National Research Foundation of Korea (NRF) funded by the Ministry of Education (2019R1A6A3A13097301). Also, this work was supported by Institute of Information & communications Technology Planning & Evaluation (IITP) grant funded by the Korea government (MSIT) (2020-0-01389, Artificial Intelligence Convergence Research Center (Inha University)).

References

Belušić, D., Grisogono, B., Klaić, Z.B., 2007. Atmospheric origin of the devastating coupled air-sea event in the east Adriatic. J. Geophys. Res. Atmos. 112, 1–14. https://doi.org/10.1029/2006JD008204.

Chen, Y., Niu, X., 2018. Forced wave induced by an atmospheric pressure disturbance moving towards shore. Continent. Shelf Res. 160, 1–9. https://doi.org/10.1016/j.csr.2018.03.007.

Choi, B.-J., Park, Y.-W., Kwon, K.-M., 2008. Generation and growth of long ocean waves along the west coast of Korea in March 2007. Ocean Polar Res. 30, 453–466. https://doi.org/10.4217/OPR.2008.30.4.453.

Choi, J.-Y., Lee, D.-Y., 2009. Analysis of small-scale atmospheric pressure jumps related to the generation of abnormal extreme waves at Boryeong. Ocean Polar Res. 31, 379–388.

Churchill, D.D., Houston, S.H., Bond, N.A., 1995. The Daytona Beach wave of 3–4 July 1992: a shallow-water gravity wave forced by a propagating squall line. Bull. Am. Meteorol. Soc. 76, 21–32. https://doi.org/10.1175/1520-0477(1995)076<0021:tdbwoj>2.0.co;2.

Dusek, G., DiVeglio, C., Licate, L., Heilman, L., Kirk, K., Paternostro, C., Miller, A., 2019. A meteotsunami climatology along the U.S. East Coast. Bull. Am. Meteorol. Soc. 100, 1329–1345. https://doi.org/10.1175/BAMS-D-18-0206.1.

Eom, H.-M., Seung, Y.-H., Woo, S.-B., You, S.-H., 2012. Analysis of abnormal wave at the west coast on 31 March 2007. J. Korean Soc. Coast. Ocean Eng. 24, 217–227. https://doi.org/10.9765/kscoe.2012.24.3.217.

Garcies, M., Gomis, D., Monserrat, S., 1996. Pressure-forced seiches of large amplitude in inlets of the Balearic Islands: 2. Observational study. J. Geophys. Res. Oceans. 101, 6453–6467. https://doi.org/10.1029/95JC03626.

Gomis, D., Monserrat, S., Tintore, J., 1993. Pressure-forced seiches of large amplitude in inlets of the Balearic Islands. J. Geophys. Res. Oceans. 98, 14437–14445. https://doi.org/10.1029/93jc00623.

Gossard, E.E., Hooke, W.H., 1975. Waves in the Atmosphere. Elsevier, New York, p. 456. http://www.scirp.org/(S(lz5mqp453edsnp55rrgjct55))/reference/ReferencesPapers.aspx?ReferenceID=1256805.

Grinsted, A., Moore, J.C., Jevrejeva, S., 2004. Application of the cross wavelet transform and wavelet coherence to geophysical time series. Nonlinear Process Geophys. 11, 561–566. https://doi.org/10.5194/npg-11-561-2004.

Hibiya, T., Kajiura, K., 1982. Origin of the Abiki phenomenon (a kind of seiche) in Nagasaki bay. J. Oceanogr. Soc. Jpn. 38, 172–182. https://doi.org/10.1007/BF02110288.

Jansà, A., Monserrat, S., Gomis, D., 2007. The rissaga of 15 June 2006 in Ciutadella (Menorca), a meteorological tsunami. Adv. Geosci. 12, 1–4. https://doi.org/10.5194/adgeo-12-1-2007.

Kazeminezhad, M.H., Vilibić, I., Denamiel, C., Ghafarian, P., Negah, S., 2021. Weather radar and ancillary observations of the convective system causing the northern Persian Gulf meteotsunami on 19 March 2017. Nat. Hazards 106, 1147–1769. https://doi.org/10.1007/s11069-020-04208-0.

Kim, H., Kim, Y.-K., Woo, S.-B., Kim, M.-S., 2014. Atmospheric analysis on the meteotsunami case occurred on 31 March 2007 at the Yellow Sea of South Korea. J. Environ. Sci. Int. 23, 1999–2014. https://doi.org/10.5322/jesi.2014.23.12.1999.

Kim, M.-S., Kim, H., Kim, Y.-K., Gu, B.-H., Lee, H.-J., Woo, S.-B., 2016. Double resonance effect at Daeheuksando port caused by air pressure disturbances in Yellow Sea on 31 March 2007. J. Coast Res. 75, 1142–1146. https://doi.org/10.2112/SI75-229.1.

Kim, M.-S., Kim, H., Eom, H.-M., Yoo, S.-H., Woo, S.-B., 2019. Occurrence of hazardous meteotsunamis coupled with pressure disturbance traveling in the Yellow Sea, Korea. J. Coast Res. 91, 71–75. https://doi.org/10.2112/si91-015.1.

Kim, M.-S., Eom, H., Lim, E.-P., Lee, C.-K., You, S.-H., Woo, S.-B., 2020. Method for detection of meteotsunami propagation in the Yellow Sea: reported cases. J. Coast Res. 95, 1134–1139. https://doi.org/10.2112/SI95-220.1.

Kim, M.-S., Eom, H., You, S.-H., Woo, S.-B., 2021. Real-time pressure disturbance monitoring system in the Yellow Sea: pilot test during the period of March to April 2018. Nat. Hazards 106, 1703–1728. https://doi.org/10.1007/s11069-020-04245-9.

Linares, Á., Wu, C.H., Bechle, A.J., Anderson, E.J., Kristovich, D.A.R., 2019. Unexpected rip currents induced by a meteotsunami. Sci. Rep. 9, 2105. https://doi.org/10.1038/s41598-019-38716-2.

Marcos, M., Monserrat, S., Medina, R., Orfila, A., Olabarrieta, M., 2009. External forcing of meteorological tsunamis at the coast of the Balearic Islands. Phys. Chem. Earth 34 (17–18), 938–947. https://doi.org/10.1016/j.pce.2009.10.001.

Monserrat, S., Rabinovich, A.B., Casas, B., 1998. On the reconstruction of the transfer function for atmospherically generated seiches. Geophys. Res. Lett. 25 (12), 2197–2200. https://doi.org/10.1029/98GL01506.

Monserrat, S., Vilibić, I., Rabinovich, A.B., 2006. Meteotsunamis: atmospherically induced destructive ocean waves in the tsunami frequency band. Nat. Hazards Earth Syst. Sci. 6, 1035–1051. https://doi.org/10.5194/nhess-6-1035-2006.

Okihiro, M., Guza, R.T., Seymour, R.J., 1993. Excitation of seiche observed in a small harbor. J. Geophys. Res. Oceans. 98, 18201–18211. https://doi.org/10.1029/93jc01760.

Oltman-Shey, J., Guza, R.T., 1987. Infragravity edge wave observations on two California beaches. J. Phys. Oceanogr. 17 (5), 644–663. https://doi.org/10.1175/1520-0485(1987)017<0644:IEWOOT>2.0.CO;2.

Orlić, M., Belušić, D., Janeković, I., Pasarić, M., 2010. Fresh evidence relating the great Adriatic surge of 21 June 1978 to mesoscale atmospheric forcing. J. Geophys. Res. 115, C06011 https://doi.org/10.1029/2009JC005777.

Ozsoy, O., Haigh, I.D., Wadey, M.P., Nicholls, R.J., Wells, N.C., 2016. High-frequency sea level variations and implications for coastal flooding: a case study of the Solent, UK. Continent. Shelf Res. 122, 1–13. https://doi.org/10.1016/j.csr.2016.03.021.

Pattiaratchi, C.B., Wijeratne, E.M.S., 2009. Tide gauge observations of 2004–2007 indian ocean tsunamis from Sri Lanka and Western Australia. Pure Appl. Geophys. 166, 233–258. https://doi.org/10.1007/s00024-008-0434-5.

Pattiaratchi, C.B., Wijeratne, E.M.S., 2015. Are meteotsunamis an underrated hazard? Philos. Trans. R. Soc. A Math. Phys. Eng. Sci. 373, 20140377 https://doi.org/10.1098/rsta.2014.0377.

Proudman, J., 1929. The effects on the sea of changes in atmospheric pressure. Geophys. Suppl. Mon. Notices R. Astron. Soc. 2, 197–209. https://doi.org/10.1111/j.1365-246X.1929.tb05408.x.

Rabinovich, A.B., 1997. Spectral analysis of tsunami waves: separation of source and topography effects. J. Geophys. Res. 102 (C6), 12663–12676. https://doi.org/10.1029/97JC00479.

Rabinovich, A.B., Stephenson, F.E., 2004. Longwave measurements for the coast of British columbia and improvements to the tsunami warning capability. Nat. Hazards 32, 313–343. https://doi.org/10.1023/B:NHAZ.0000035549.26392.c8.

Rabinovich, A.B., 2009. Seiches and harbor oscillations. In: Kim, Y.C. (Ed.), Handbook of Coastal and Ocean Engineering. World Sci., Singapore, pp. 193–236. https://doi.org/10.1142/9789812819307_0009.

Rabinovich, A.B., 2020. Twenty-seven years of progress in the science of meteorological tsunamis following the 1992 daytona beach event. Pure Appl. Geophys. 177, 1193–1230. https://doi.org/10.1007/s00024-019-02349-3.

Rabinovich, A.B., Šepić, J., Thomson, R.E., 2021. The meteorological tsunami of 1 November 2010 in the southern Strait of Georgia: a case study. Nat. Hazards 106, 1503–1544. https://doi.org/10.1007/s11069-020-04203-5.

Šepić, J., Vilibić, I., Belušić, D., 2009a. Source of the 2007 ist meteotsunami (Adriatic sea). J. Geophys. Res. Oceans. 114, 1–14. https://doi.org/10.1029/2008JC005092.

Šepić, J., Denis, L., Vilibić, I., 2009b. Real-time procedure for detection of a meteotsunami within an early tsunami warning system. Phys. Chem. Earth 34, 1023–1031. https://doi.org/10.1016/j.pce.2009.08.006.

Šepić, J., Vilibić, I., 2011. The development and implementation of a real-time meteotsunami warning network for the Adriatic Sea. Nat. Hazards Earth Syst. Sci. 11, 83–91. https://doi.org/10.5194/nhess-11-83-2011.

Šepić, J., Vilibić, I., Strelec Mahović, N., 2012. Northern Adriatic meteorological tsunamis: observations, link to the atmosphere, and predictability. J. Geophys. Res. Oceans. 117, 1–18. https://doi.org/10.1029/2011JC007608.

Šepić, J., Rabinovich, A.B., 2014. Meteotsunami in the great lakes and on the Atlantic coast of the United States generated by the 'derecho' of June 29–30, 2012. Nat. Hazards 74, 75–107. https://doi.org/10.1007/s11069-014-1310-5.

Šepić, J., Vilibić, I., Fine, I., 2015a. Northern Adriatic meteorological tsunamis: assessment of their potential through ocean modeling experiments. J. Geophys. Res. Oceans. 120, 2993–3010. https://doi.org/10.1002/2015JC010795.

Šepić, J., Vilibić, I., Rabinovich, A.B., Monserrat, S., 2015b. Widespread tsunami-like waves of 23–27 June in the Mediterranean and Black Seas generated by high-Altitude atmospheric forcing. Sci. Rep. 5, 11682. https://doi.org/10.1038/srep11682.

Šepić, J., Vilibić, I., Monserrat, S., 2016. Quantifying the probability of meteotsunami occurrence from synoptic atmospheric patterns. Geophys. Res. Lett. 43, 10377–10384. https://doi.org/10.1002/2016GL070754.

Tepper, M., 1950. A proposed mechanism of squall lines: the pressure jump line. J. Meteorol. 7, 21–29. https://doi.org/10.1175/1520-0469(1950)007<0021:apmosl>2.0.co;2.

Thomson, R.E., Emery, W.J., 2014. Data Analysis Methods in Physical Oceanography, third ed. Elsevier, New York, p. 716. https://doi.org/10.1016/C2010-0-66362-0.

Thotagamuwage, D.T., Pattiaratchi, C.B., 2014. Observations of infragravity period oscillations in a small marina. Ocean Eng 88, 435–445. https://doi.org/10.1016/j.oceaneng.2014.07.003.

Torrence, C., Compo, G.P., 1998. A practical guide to wavelet analysis. Bull. Am. Meteorol. Soc. 79, 61–78. https://doi.org/10.1175/1520-0477(1998)079<0061:APGTWA>2.0.CO;2.

Vilibić, I., Domijan, N., Orlić, M., Leder, N., Pasarić, M., 2004. Resonant coupling of a traveling air pressure disturbance with the east Adriatic coastal waters. J. Geophys. Res. Oceans. 109, 1–13. https://doi.org/10.1029/2004JC002279.

Vilibić, I., 2008. Numerical simulations of the Proudman resonance. Continent. Shelf Res. 28, 574–581. https://doi.org/10.1016/j.csr.2007.11.005.

Vilibić, I., Monserrat, S., Rabinovich, A.B., 2014. Meteorological tsunamis on the US East Coast and in other regions of the world ocean. Nat. Hazards 74, 1–9. https://doi.org/10.1007/s11069-014-1350-x.

Vilibić, I., Šepić, J., Dunić, N., Sevault, F., Monserrat, S., Jordà, G., 2018. Proxy-based assessment of strength and frequency of meteotsunamis in future climate. Geophys. Res. Lett. 45, 10501–10508. https://doi.org/10.1029/2018GL079566.

Welch, P.D., 1967. The use of fast Fourier transform for the estimation of power spectra: a method based on time averaging over short, modified periodograms. IEEE Trans. Audio Electroacoust. 15, 70–73. https://doi.org/10.1109/TAU.1967.1161901.

Wilson, B.W., 1972. Seiches. Adv. Hydrosci. 8, 1–94. https://doi.org/10.1016/B978-0-12-021808-0.50006-1.